JOURNAL OF GUIDANCE, CONTROL, AND DYNAMICS
Vol. 34, No. 3, May–June 2011

Rock-Around Orbits

Scott K. Bourgeois* and Daniele Mortari†
Texas A&M University, College Station, Texas 77843

DOI: 10.2514/1.51085

A new class of orbits, called rock-around orbits, which are compatible to an assigned target orbit, is presented. These orbits allow the design of systems whose purpose is to explore and/or observe the space around an assigned target orbit. The proposed orbit design guarantees that, within a given repetition time, the whole space around the target orbit is observed under a prescribed maximum observation distance constraint. Potential applications can be civilian, to design orbits for mapping and monitoring systems, as well as military, to design orbits for space-based surveillance systems. This study shows how to design rock-around orbits for circular and elliptical target orbits, how to evaluate the observation efficiency, and how to estimate the orbit maintenance costs.

I. Introduction

THE problem of providing reliable surveillance systems to detect space threats to international space assets has recently and voluminously increased. This problem involves military as well as civilian and scientific fields. Space surveillance systems tasks involve detecting, tracking, cataloging, and identifying the objects orbiting Earth. A large class of these objects are now inactive, such as dead satellites, spent rocket bodies, and a huge variety of fragmentation debris. About 7% of the space objects are operational satellites, the rest are debris. These threats are located in a range going from low Earth orbit (LEO) to the geostationary (GEO) belt.

To monitor the space and guarantee a sufficient level of safety, several space agencies have collected their funds to build a network that could achieve this critical goal. The Space Surveillance Network (SSN) of the U.S. Army, Navy, and Air Force, is the first space-based surveillance system with ground-based radar's and optical sensors at 25 sites worldwide. The SSN [1–5] has been efficiently tracking space objects since 1957.

However, in order to design an efficient space-based surveillance system the observing satellites orbits should be "synchronized" with the orbits of the assigned assets. This synchronization is particularly important for the GEO belt where the space assets are not uniformly distributed along the belt but are located in positions mainly depending on the communications constraints (e.g., frequency allocation, pointing, etc.). This synchronization is here introduced as a mandatory constraint by forcing the observing satellite orbit to be compatible (resonant) with an assigned target orbit. To obtain this result we mimic the theory of flower constellations [6–9], by replacing the compatibility with Earth's spin rate by the compatibility with target orbit's mean motion. The theory of flower constellations has generated many byproducts [10,11] and many potential solutions for Earth and space observing systems. In particular, the ability to obtain or design symmetric periodic solutions makes the theory an attractive tool to design either Earth reconnaissance systems as well as space-based surveillance systems. While Earth reconnaissance missions require the synchronization be relative to the Earth's spin period the space surveillance missions of certain orbits/regions (e.g., GEO belt, LEO, multistationary orbits, etc.) require the synchronization be relative to the orbital period of the target orbit.

Additional motivations to investigate, observe, and monitor the space around the space surrounding a given orbit come from civilian and/or scientific applications. The possibility to map Earth's magnetic and gravity fields and to monitor physical quantities (e.g., protons, ions, etc.) in certain important space regions (equatorial, polar, etc.) are just two examples of the potential applications list.

An orbit is defined by five orbital parameters: semimajor axis (a), eccentricity (e), right ascension of ascending node (Ω), inclination (i), and argument of perigee (ω). The first two parameters determine the shape of the orbit while the remaining three determine the spatial orientation. This study shows how to design these parameters to obtain rock-around orbits (RAOs, identified by subscript "r") [12,13], which are producing relative trajectories (in the target orbit's rotating frame) spiralling around the assigned target orbit (identified by subscript "t") and periodically observing the volume around the target orbit under maximum distance constraint. The circular and elliptical target orbits are both considered. The term *rock-around* refers to the spiralling motion of the spacecraft as it moves around the target orbit. Because of the difference in semimajor axis, eccentricity, and inclination, the satellite will travel inside, outside, above and below the target orbit. The satellite will essentially spiral around the target orbit, hence the rock-around motion.

II. Circular Target Orbits

This section analyzes the target circular orbit case by introducing the admissible orbits (satisfying the distance constraint) and the compatible orbits (satisfying the orbital synchronization).

A. Admissible Orbits

Let a_t be the semimajor axis of the target circular orbit. To maintain the RAO within a $d_{\max}$ distance from the target orbit the RAO semimajor axis, a_r, must satisfy the bounds

$$a_t - d_{\max} \leq a_r \leq a_t + d_{\max} \tag{1}$$

This allows a spacecraft to observe the entire target orbit in the amount of time

$$T_{\text{rep}} = \frac{T_t}{|T_t - T_r|} T_r = N_r T_r \tag{2}$$

where N_r is the number of RAO periods completed during the repetition time, T_{rep}, and where T_r and T_t are the RAO and the target orbital periods, respectively. For an assigned maximum repetition time, $T_{\text{rep max}}$, the observation time is bounded by

$$N_r T_r \leq T_{\text{rep max}} \tag{3}$$

Substituting Eq. (2) in Eq. (3) and solving for T_r, the following bounds for T_r,

Presented as Paper 2009-343 at the AAS/AIAA Astrodynamics Specialist Conference, Pittsburgh, PA, 9–13 August 2009; received 29 June 2010; revision received 4 December 2010; accepted for publication 6 December 2010.

*Graduate Student, Aerospace Engineering, 3141 TAMU; sbourgeois@tamu.edu.

†Associate Professor, Aerospace Engineering, 746C H. R. Bright Building, 3141 TAMU; mortari@tamu.edu. Associate Fellow AIAA.

$$T_r \le \frac{T_t T_{\text{rep max}}}{T_t + T_{\text{rep max}}} \quad (\text{for } T_r < T_t) \quad \text{and}$$
$$T_r \ge \frac{T_t T_{\text{rep max}}}{T_{\text{rep max}} - T_t} \quad (\text{for } T_r > T_t) \tag{4}$$

are obtained. Using Kepler's third law, $T_r = 2\pi\sqrt{a_r^3/\mu}$, the semimajor axis

$$a_r = \sqrt[3]{\mu\left(\frac{T_r}{2\pi}\right)^2} \tag{5}$$

can be evaluated. Finally, combining Eq. (5) with Eq. (1), the bounds for a_r,

$$\begin{cases} a_t - d_{\max} \le a_r \le \sqrt[3]{\mu\left(\frac{1}{2\pi}\frac{T_t T_{\text{rep max}}}{T_t + T_{\text{rep max}}}\right)^2} & (\text{for } a_r < a_t) \\ a_t + d_{\max} \ge a_r \ge \sqrt[3]{\mu\left(\frac{1}{2\pi}\frac{T_t T_{\text{rep max}}}{T_{\text{rep max}} - T_t}\right)^2} & (\text{for } a_r > a_t) \end{cases} \tag{6}$$

are obtained.

B. Compatible Orbits

The approach previously described is suitable to observe target orbits with uniformly distributed interest. Specific interests and preferences exist in those situations in which one wants to observe assigned distributions of space assets and wants to make sure the RAO spacecraft will always be in the same position relative to those objects. To obtain these repeating space trajectories the compatible (resonant) orbit constraint must be add to the admissible constraint.

An orbit is called compatible with respect to a rotating reference frame if there exist two integers, $N_r \in \mathbb{Z}(1)$ and $N_t \in \mathbb{Z}(1)$, satisfying

$$N_r T_r = N_t T_t = T_{\text{rep}} \le T_{\text{rep max}} \tag{7}$$

Once T_r is known, the RAO semimajor axis can be computed using Eq. (5):

$$a_r = \sqrt[3]{\mu\left(\frac{N_t T_t}{2\pi N_r}\right)^2} \tag{8}$$

To satisfy $T_{\text{rep}} \le T_{\text{rep max}}$, a limited number of the $[N_r, N_t]$ integer combination pairs are available. From $T_{\text{rep max}}$, we can derive an upper value for the maximum allowable target orbital periods to observe the target orbit once, $N_{t\max} = T_{\text{rep max}}/T_t$. Additional bounds can be derived from maintaining the observation resolution within the requirements of the observation accuracy, $d \le d_{\max}$. As an example, Fig. 1 shows all the possible $[N_r, N_t]$ combinations of a scenario for which the target orbit is the GEO orbit, whose parameters are $T_t = 24$ h, $a_t = 42,164$ km, $e_t = 0$, $\Omega_t = 0°$, $i_t = 0°$, $\omega_t = 0°$, $d_{\max} = 5000$ km, and $T_{\text{rep max}} = 30$ days.

Figure 1 includes the three lines identifying the bounds defined by $d_{\max}$ and $N_{t\max}$. This figure also shows that the number of possible combination pairs $[N_r, N_t]$ increases by increasing $N_{t\max}$ and/or by increasing $d_{\max}$.

C. Eccentricity and Inclination Bounds

Based on the $d_{\max}$ limit, perigee and apogee bounds of the RAO can be derived for any assigned target orbit. The eccentricities associated with these bounds can be evaluated for all the compatible orbits (provided in Fig. 1) using the semimajor axis obtained from Eq. (8). For orbits with $a_r < a_t$, the apogee must be greater than the radius of the target orbit to ensure the rock-around motion and the perigee must be greater than $a_t - d_{\max}$ to ensure it is within the $d_{\max}$ distance from the target orbit. Similarly, for the orbits where $a_r > a_t$, the perigee must be lower than the radius of the target orbit and the apogee must be lower than $a_t + d_{\max}$.

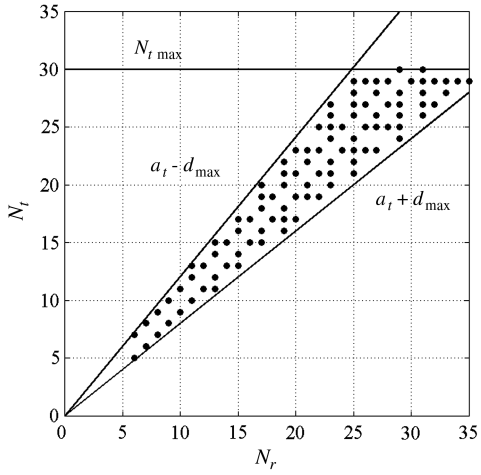

Fig. 1 Admissible values of N_r and N_t for example 1 (circular target orbit).

The expressions for perigee and apogee radii are

$$R_p = a_r(1 - e_r) \quad \text{and} \quad R_a = a_r(1 + e_r) \tag{9}$$

The R_p and R_a radii expressions are then used to compute the eccentricity bounds

for $a_r < a_t$:

$$\begin{cases} a_t = R_a = a_r(1 + e_{\min}) & \rightarrow e_{\min} = \dfrac{a_t}{a_r} - 1 \\ a_t - d_{\max} = R_p = a_r(1 - e_{\max}) & \rightarrow e_{\max} = 1 - \dfrac{a_t - d_{\max}}{a_r} \end{cases} \tag{10}$$

and

for $a_r > a_t$:

$$\begin{cases} a_t = R_p = a_r(1 - e_{\min}) & \rightarrow e_{\min} = 1 - \dfrac{a_t}{a_r} \\ a_t + d_{\max} = R_a = a_r(1 + e_{\max}) & \rightarrow e_{\max} = \dfrac{a_t + d_{\max}}{a_r} - 1 \end{cases} \tag{11}$$

where if $e_{\min} < 0$ then $e_{\min} = 0$ is adopted as the eccentricity cannot be negative. Summarizing, the eccentricity bounds are

$$\text{for } a_r < a_t\text{: } \frac{a_t}{a_r} - 1 \le e_r \le 1 - \frac{a_t - d_{\max}}{a_r}$$
$$\text{for } a_r > a_t\text{: } 1 - \frac{a_t}{a_r} \le e_r \le \frac{a_t + d_{\max}}{a_r} - 1 \tag{12}$$

As for the inclination, the bounds are derived from the knowledge of $d_{\max}$ and e_r. Figure 2 shows the geometry in the plane identified by the normal to the target orbit and to the RAO's apsidal line. This figure shows the perigee and apogee relative positions of the RAO, R_p and R_a, and the inclination difference, Δi, between target and RAOs.

Figure 2 clearly shows that the maximum inclination difference is found when R_p or R_a touches the $d_{\max}$-radius circle (section of a torus). The equation of this circle is $(x - a_t)^2 + y^2 = d_{\max}^2$. The two

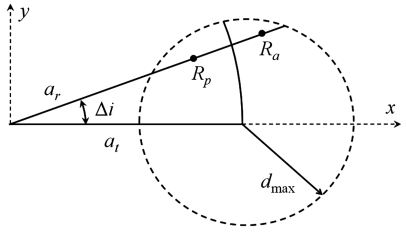

Fig. 2 Inclination bounds geometry for a circular target orbit.

extreme conditions on R_p or R_a, whose values are provided in Eq. (9), yields to

$$\begin{cases} x = R_a \cos \Delta i \\ y = R_a \sin \Delta i \end{cases} \quad \text{and} \quad \begin{cases} x = R_p \cos \Delta i \\ y = R_p \sin \Delta i \end{cases}$$

respectively. From these equations Δi can be found as a function of e_r. Thus, obtaining

$$\cos \Delta i(R_a) = \frac{d_{\max}^2 - a_r^2(1+e_r)^2 - a_t^2}{-2a_r(1+e_r)a_t} \quad \text{and}$$
$$\cos \Delta i(R_p) = \frac{d_{\max}^2 - a_r^2(1-e_r)^2 - a_t^2}{-2a_r(1-e_r)a_t}$$

It is trivial to prove that $\Delta i(R_a)$ holds for $a_r > a_t$ while $\Delta i(R_p)$ holds for $a_r < a_t$, respectively. Hence, the inclination bounds are

$$i_{\min} = i_t - \Delta i \le i_r \le i_t + \Delta i = i_{\max} \tag{13}$$

and finally we obtain the expressions for Δi:

$$\begin{aligned} &\text{for } a_r < a_t\text{: } \Delta i = \cos^{-1}\left[\frac{d_{\max}^2 - a_r^2(1-e_r)^2 - a_t^2}{-2a_r(1-e_r)a_t}\right] \\ &\text{for } a_r > a_t\text{: } \Delta i = \cos^{-1}\left[\frac{d_{\max}^2 - a_r^2(1+e_r)^2 - a_t^2}{-2a_r(1+e_r)a_t}\right] \end{aligned} \tag{14}$$

While using the preceding procedure, two important facts must be taken into consideration:

1) Orbit inclination is always positive. Therefore, if $i_{\min} < 0$, then it means that the ascending node and descending node have swapped positions which is a 180° change in Ω. So the true bounds become: $0 \le i_r \le i_{\max}$ for Ω_r and $0 \le i_r \le |i_{\min}|$ for $\Omega_r \pm 180°$.

2) Equations (13) and (14) are valid for any value of the RAO's argument of perigee. However, large inclination differences can also be achieved by changing the RAO's argument of perigee. This is due to the fact that for a circular target orbit, a RAO is at its greatest distance from the target orbit at either the apogee or perigee. If the RAO argument of perigee is 90 or 270°, the apogee and perigee are at the antinodes, the highest and lowest part of the orbit. This maximizes the distance from the target orbit. If the RAO argument of perigee is 0 or 180°, then the RAO apogee and perigee are at the ascending and descending nodes, minimizing the distance from the target orbit. This is clearly shown in Fig. 3, providing the RAO to GEO distance in the GEO rotating frame. This example uses the target orbit parameters defined in Sec. II.B and the RAO parameters defined as $N_r = 23$, $N_t = 24$, $T_r = 22.79$ h, $a_r = 40,815$ km, $e_{r\min} = 0.0331$, and $e_{r\max} = 0.0894$.

D. Example

To better understand how a RAO works, the trajectory of the RAO spacecraft has to be seen in the rotating target orbit frame. For this purpose, the coordinate transformation matrices between inertial, rotating target, and RAO frames must be introduced. Using the "3-1-3" Euler's sequence to move from a reference frame to another, the transformation matrix moving from inertial to the RAO frame is

$$C_{i2r} = C_3(\omega_r)C_1(i_r)C_3(\Omega_r) \tag{15}$$

and the inertial to rotating target transformation matrix is

$$C_{i2t} = C_3(\omega_t + \varphi_t)C_1(i_t)C_3(\Omega_t) \tag{16}$$

where

$$C_1(\vartheta) = \begin{bmatrix} 1 & 0 & 0 \\ 0 & \cos\vartheta & \sin\vartheta \\ 0 & -\sin\vartheta & \cos\vartheta \end{bmatrix} \quad \text{and}$$
$$C_3(\vartheta) = \begin{bmatrix} \cos\vartheta & \sin\vartheta & 0 \\ -\sin\vartheta & \cos\vartheta & 0 \\ 0 & 0 & 1 \end{bmatrix}$$

are the matrices performing rigid rotation about first and third coordinate axes, respectively, and φ_t represents the true anomaly of a reference fictitious spacecraft in the target orbit frame. Equations (15) and (16) allow us to evaluate the RAO-to-target transformation matrix

$$C_{r2t} = C_{i2t}C_{r2i} = C_{i2t}C_{i2r}^T \tag{17}$$

Therefore, the relative motion of the RAO spacecraft in the target orbit frame is described by the vector

$$\mathbf{R}_r^{(t)} = \{ x_r^{(t)}, \quad y_r^{(t)}, \quad z_r^{(t)} \}^T = C_{r2t}\mathbf{R}_r^{(r)} = C_{i2t}\mathbf{R}_r^{(i)} \tag{18}$$

where $\mathbf{R}_r^{(i)}$, $\mathbf{R}_r^{(t)}$, and $\mathbf{R}_r^{(r)}$, indicate the RAO spacecraft position vector in the inertial, target, and RAO reference frames, respectively.

Using the GEO orbit as a target orbit (as defined in Sec. II.B), consider the prograde ($N_r > N_t$) and retrograde ($N_r < N_t$) RAO scenarios, whose bounds and selected orbital parameters are provided in Table 1.

For the two RAO scenarios selected in this example, Fig. 4 shows the GEO and RAO as projected on the GEO orbital plane while Fig. 5 shows the three-dimensional views of the RAO trajectories as appearing in the rotating GEO reference frame. Figure 5 clearly shows the prograde and retrograde spiraling trajectories of the two RAOs around the GEO orbit.

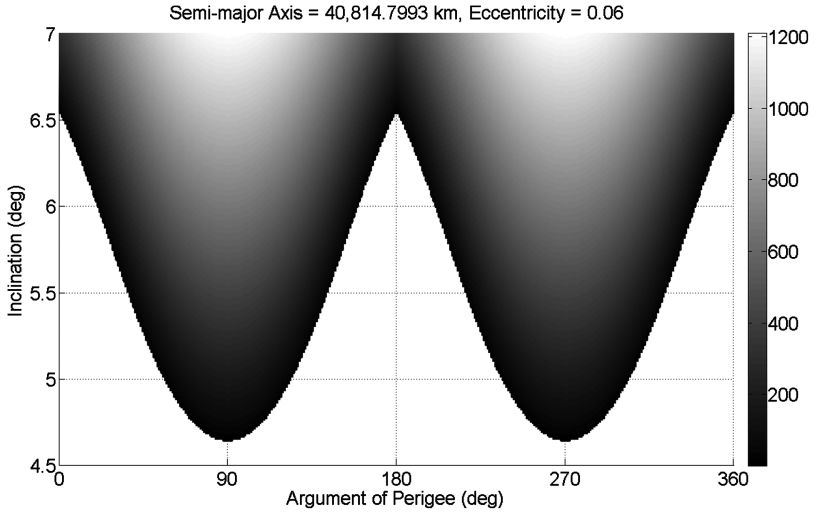

Fig. 3 RAO to GEO distance in the rotating GEO frame: top view (example 1).

Table 1 Eccentricity bounds and orbital parameters for two selected RAO satellites

Scenario	N_r	N_t	T_r, hr	a_r, km	$e_{r\min}$	$e_{r\max}$	e_r	Ω_r, deg	i_r, deg	ω_r, deg
Prograde	25	24	22.98	41,032	0.0276	0.0943	0.0943	0.0	5.75	0.0
Retrograde	24	25	24.93	43,327	0.0268	0.0886	0.0886	0.0	5.75	0.0

Both prograde and retrograde RAO have "loops" in which the observer covers a portion of the GEO belt. The number of these loops (also called *petals* in the flower constellation theory) is controlled by the selected $[N_r, N_t]$ integers pair. The size of these loops can increase or decrease by changing the eccentricity and the inclination of the RAO. It is also of interest to note that the RAO with a semimajor axis greater than that of the GEO belt (retrograde RAO) spends more time outside the belt than inside while the opposite occurs for RAOs with smaller semimajor axes (prograde RAO).

E. Minimum Distance

The minimum distance to the target orbit, $d_{\min}$, is a quantity of particular interest. For instance, to obtain uniform observation distance optimality could be defined as the one maximizing $d_{\min}$ (see Fig. 5). To evaluate $d_{\min}$ the RAO trajectory must be evaluated in the fixed (not rotating) target reference frame. To this end, the inertial-to-target orbit transformation matrix

$$C_{i2t} = C_3(\omega_t)C_1(i_t)C_3(\Omega_t) \tag{19}$$

must be computed. Using Eqs. (15) and (17–19), the RAO trajectory in the fixed target orbit reference frame can be obtained. Let $\{x_r^{(t)}, \quad y_r^{(t)}, \quad 0\}^T$ be the projection vector of the RAO position onto the target orbit plane. Therefore, the distance between the projection and the target orbit is simply the radial distance to the projection minus the radius (or semimajor axis) of the target orbit. As shown in Fig. 6, this distance, the out-of-plane component $z_r^{(t)}$, and $d_{\min}$, form the three sides a right triangle with $d_{\min}$ as the hypotenuse. Therefore, we have $d_{\min} = \sqrt{(\sqrt{x_r^{(t)2} + y_r^{(t)2}} - a_t)^2 + z_r^{(t)2}}$.

Figure 7 provides the minimum distance to the GEO orbit in one RAO period T_r. As it can be seen, the RAO is always within the $d_{\max}$ boundary while using the maximum allowed eccentricity and inclination.

III. Elliptical Target Orbits

Finding RAOs for elliptical target orbits is slightly different than for circular target orbits since the radius of the target orbit is no longer a constant.

A. Admissible and Compatible Orbits

The process for finding admissible and compatible orbits for the elliptical case is the same as described in the circular case. The target orbit parameters in this example are $T_t = 22.12$ h, $a_t = 40,000$ km, $e_t = 0.5$, $\Omega_t = 0°$, $i_t = 0°$, $\omega_t = 0°$, $d_{\max} = 5000$ km, and $N_{d_{\max}} = 30$ days, while Fig. 8 shows the $[N_r, N_t]$ integer pairs associated with the admissible and compatible orbits.

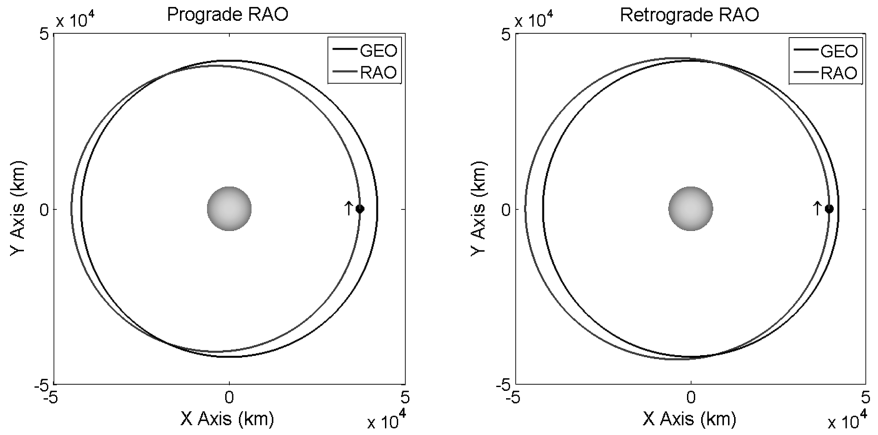

Fig. 4 Prograde and retrograde RAOs (from inertial reference frame).

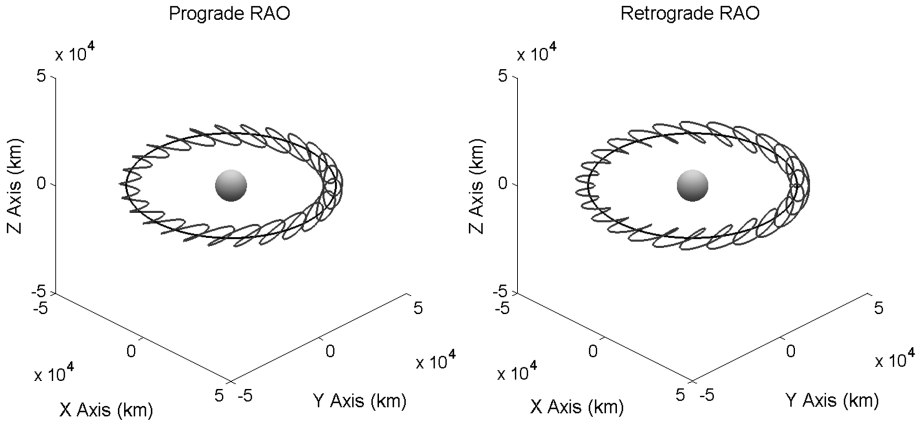

Fig. 5 Prograde and retrograde RAO trajectories (three-dimensional view in the rotating GEO frame).

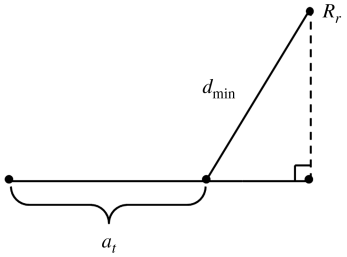

Fig. 6 Minimum distance geometry to the target orbit.

B. Eccentricity Bounds

Also in the elliptical case, to satisfy the distance constraints the RAO should be no farther than $d_{\max}$ from perigee and apogee. Using Eq. (9) and solving it for the minimum and maximum eccentricities yields to the following bounds:

$$\text{for } a_r < a_t\text{: } e_2 = \frac{R_a - d_{\max}}{a_r} - 1 \le e_r \le 1 - \frac{R_p - d_{\max}}{a_r} = e_4$$
$$\text{for } a_r > a_t\text{: } e_3 = 1 - \frac{R_p + d_{\max}}{a_r} \le e_r \le \frac{R_a + d_{\max}}{a_r} - 1 = e_1 \tag{20}$$

The values of the eccentricity bounds (e_1 through e_4), as provided by Eq. (20), are plotted in Fig. 9. This figure also includes, as vertical lines, the values of the admissible and compatible semimajor axes shown in Fig. 8.

The effects of $d_{\max}$ can directly be derived from Eq. (20). Increasing $d_{\max}$ causes the different e_k lines to move away from the center, thus increasing the area between them. Decreasing $d_{\max}$ causes the e_k lines to constrict, thus decreasing the area between them. Increasing the value of $N_{t\max}$ increases the number of possible semimajor axes with an increase of semimajor axes with periods closer to that of the target orbit. This can be seen in Fig. 9 where the number of vertical lines become more dense toward the value of the target semimajor axis. Decreasing $N_{t\max}$ has the opposite effect.

Equations (20) provide bounds on the eccentricity values without saying anything about the optimal value. For each compatible semimajor axis the optimal eccentricity is defined as the one maximizing the observation coverage. Figure 10 shows for the coplanar ($i_t = i_r$) case and for $\omega_t = \omega_r$ the percentage of time (normalized to 1) that a spacecraft in the associated RAO is within the $d_{\max}$ boundary of the target orbit. Nearly all of the area defined by the four intersections of the eccentricities has a 100% rating. The eccentricities e_1, e_3, and their intersection along with e_2, e_4, and their intersection bound the two regions where the RAO spacecraft is never within range of the target orbit. The 100% region becomes more tightly bounded as the target orbit's eccentricity decreases until it is zero at which point it is completely bounded by e_1 and e_2. The

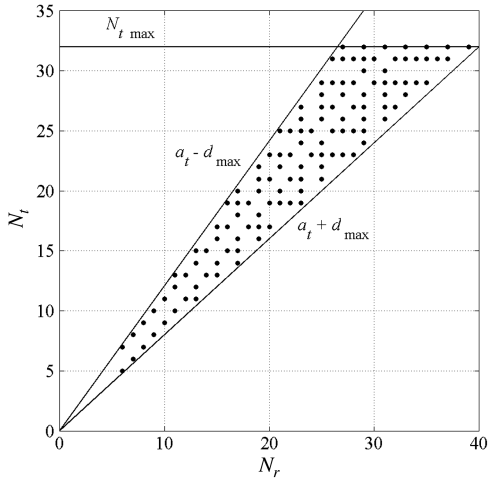

Fig. 8 Compatible orbits pairs, $[N_r, N_t]$, for elliptical target orbit (example 2).

opposite happens when the eccentricity of the target orbit increases allowing more results with a percentage rating of less than 100% into the area defined by the four intersections of the eccentricities. This still leaves a wide range of potential eccentricity values for some of the RAO semimajor axes. Even though the target and RAOs are both eccentric, the RAO eccentricity value must be sufficiently far from the target orbit's eccentricity to have the spiraling relative motion.

From the apogee and perigee radius definitions given in Eq. (9) two new values for the eccentricities,

$$e_5 = \frac{R_a}{a_r} - 1 \quad \text{and} \quad e_6 = 1 - \frac{R_p}{a_r} \tag{21}$$

are obtained to perform the spiraling relative motion. The e_5 and e_6 lines are shown in Fig. 11. These lines highlight interesting regions. For a RAO with an elliptical target orbit one of the two following conditions must apply to ensure the rock-around motion:

1) The RAO apogee must be greater than the target apogee and the RAO perigee smaller than the target perigee.

2) The RAO apogee must be smaller than the target apogee and the RAO perigee greater than the target perigee.

For $a_r < a_t$ this can be seen above e_5 and below e_6 while for $a_r > a_t$ this applies above e_6 and below e_5. Of the 100% region from Fig. 10, only the shaded areas in Fig. 11 exhibit the spiraling relative motion. This removes many of the compatible semimajor axes and reduces the eccentricity range of those that remain. Combining Eqs. (20) and (21) the final piecewise eccentricity bounds for an elliptical target orbit is obtained:

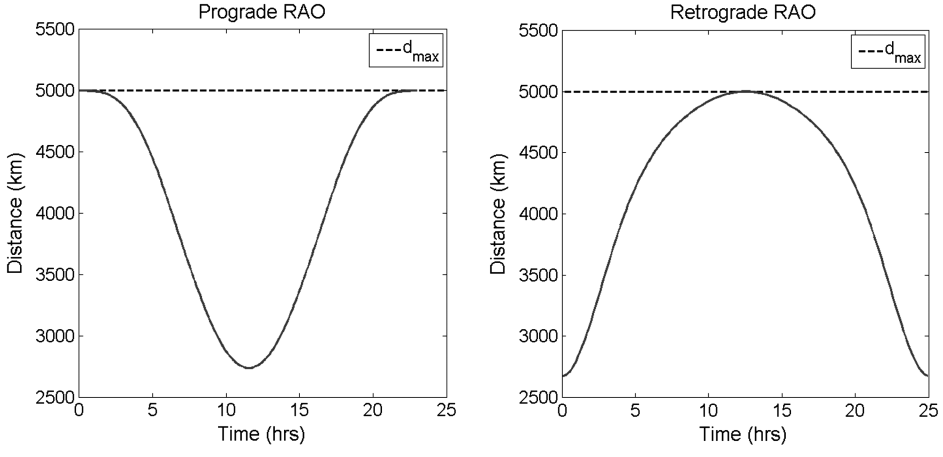

Fig. 7 Minimum distance to GEO for retrograde and prograde RAOs.

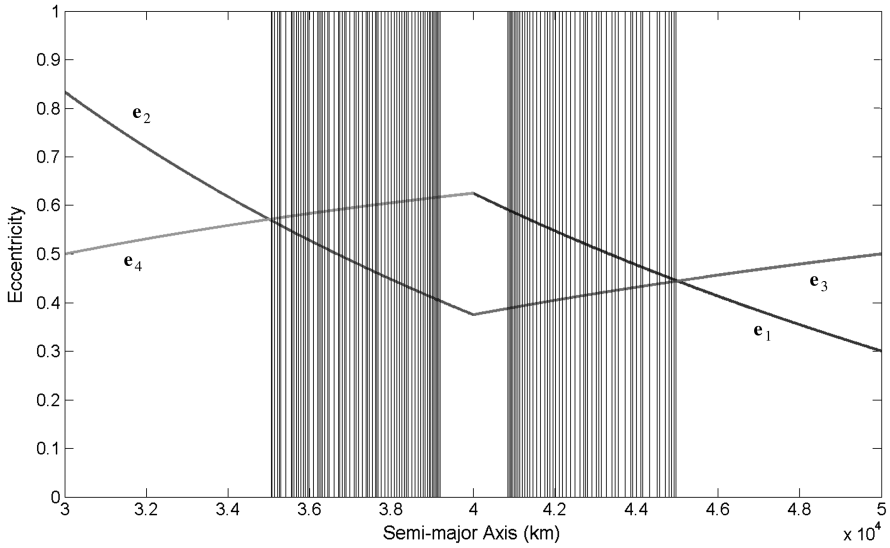

Fig. 9 Eccentricity bounds (associated to $d_{\max}$) with compatible semimajor axes (example 2).

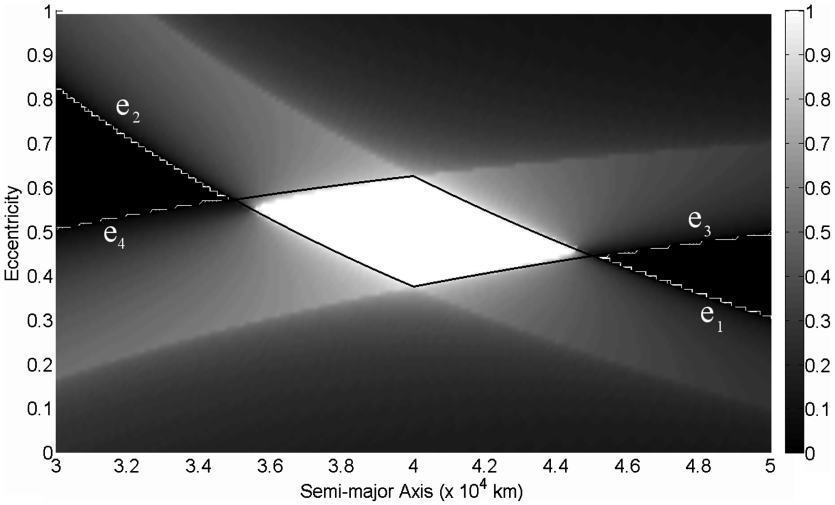

Fig. 10 Percentage of time a spacecraft in a RAO is within $d_{\max}$ of the target orbit (example 2).

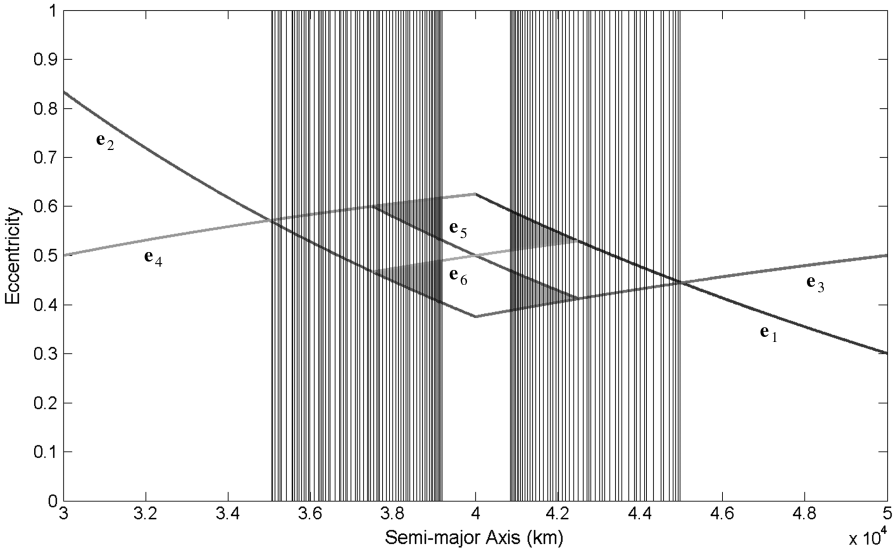

Fig. 11 All RAO eccentricity bounds and valid solutions (example 2).

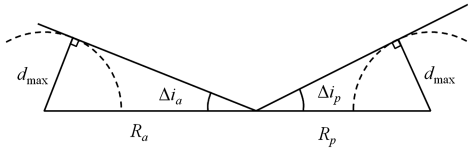

Fig. 12 Inclination bounds geometry for an elliptical reference orbit.

$$\text{for } a_r < a_t\text{: } \frac{R_a - d_{\max}}{a_r} - 1 \le e_r \le 1 - \frac{R_p}{a_r} \quad \text{and}$$
$$\frac{R_a}{a_r} - 1 \le e_r \le 1 - \frac{R_p - d_{\max}}{a_r}$$
$$\text{for } a_r > a_t\text{: } 1 - \frac{R_p + d_{\max}}{a_r} \le e_r \le \frac{R_a}{a_r} - 1 \quad \text{and}$$
$$1 - \frac{R_p}{a_r} \le e_r \le \frac{R_a + d_{\max}}{a_r} - 1 \tag{22}$$

C. Inclination Bounds

Inclination bounds for elliptical target orbit differ from those obtained for circular as the orbit target radius is not constant anymore. Figure 12 shows that there are two possible Δi values, one for the apogee and one for the perigee of the target orbit.

Since $R_a > R_p$, it follows that $\Delta i_a < \Delta i_p$. Using Δi_a ensures that the spacecraft in the RAO will be within the $d_{\max}$ boundary over the whole target orbit including the perigee whereas using Δi_p would allow the spacecraft to travel out of the $d_{\max}$ boundary over the target orbit's apogee; hence $\Delta i = \Delta i_a$. Substituting R_a of the target orbit into a_t of Eq. (14) the inclination bounds

$$i_{\min} = i_t - \Delta i \le i_r \le i_t + \Delta i = i_{\max} \tag{23}$$

are obtained, where

$$\text{for } a_r < a_t\text{: } \Delta i = \cos^{-1}\left[\frac{d_{\max}^2 - a_r^2(1-e_r)^2 - a_t^2}{-2a_r(1-e_r)a_t(1+e_t)}\right]$$
$$\text{for } a_r > a_t\text{: } \Delta i = \cos^{-1}\left[\frac{d_{\max}^2 - a_r^2(1+e_r)^2 - a_t^2}{-2a_r(1+e_r)a_t(1+e_t)}\right] \tag{24}$$

D. Example

This example considers an elliptical target orbit and a RAO whose parameters are $N_t = 13$, $T_t = 22.12$ h, $a_t = 40,000$ km, $e_t = 0.1$, $\Omega_t = 0°$, $i_t = 0°$, $\omega_t = 0°$, $d_{\max} = 5000$ km, and $N_{d_{\max}} = 30$ days; and $N_r = 14$, $T_r = 20.54$ h, $a_r = 38,072$ km, $e_r = 0.1857$, $\Omega_r = 0°$, $i_r = 4.75°$, $\omega_r = 0°$, $e_2 = 0.0244$, $e_6 = 0.0544$, $e_5 = 0.1557$, and $e_4 = 0.1857$. Like in the circular case also in the elliptical case the angular velocity of the rotating reference frame is the mean motion of the target reference frame. Figure 13 shows the target and RAO in the inertial and rotating frames, respectively. Since for an elliptical orbit $\varphi \neq M$, the target orbit cannot be seen fixed in the rotating frame like in the circular target orbit case. This makes more difficult to understand the RAO spacecraft motion in the target orbit reference frame. However, when the RAO satellite is at its apogee it is surveying the target orbit near apogee and similarly so for perigee. Furthermore, since $N_r = 14$, the RAO spacecraft covers in average $1/14$ of the target orbit in one RAO period.

E. Minimum Distance

As done for the circular case to evaluate the minimum distance, $d_{\min}$, the target orbit's reference frame is selected. However, since distances are scalars their values do not dependent from the chosen reference frame. To simplify the elliptical case problem the radius vectors are conveniently written with respect to the orbit main axes, with center at the orbit center, and not at the focus. The RAO position vector in this reference frame is identified with superscript "(t)" and is given by

$$\mathbf{R}_r^{(t)} = C_{i2t}\mathbf{R}_r^{(i)} + \begin{Bmatrix} a_t e_t \\ 0 \\ 0 \end{Bmatrix} = \begin{Bmatrix} x_r^{(t)} \\ y_r^{(t)} \\ z_r^{(t)} \end{Bmatrix} \tag{25}$$

For simplicity, let us define $u = x_r^{(t)}$ and $v = y_r^{(t)}$. The equation of the target orbit is simply

$$\frac{x^2}{a_t^2} + \frac{y^2}{b_t^2} = 1 \tag{26}$$

The closest point of the ellipse from (u, v) must be such that the point $(u - x, v - y)$ belongs to the normal of the ellipse passing through the closest point. The normal of the ellipse is

$$\nabla\left(\frac{x^2}{a_t^2} + \frac{y^2}{b_t^2} - 1\right) = \left(\frac{2x}{a_t^2}, \frac{2y}{b_t^2}\right)$$

Therefore, we can set

$$(u - x, v - y) = t\left(\frac{x}{a_t^2}, \frac{y}{b_t^2}\right) \tag{27}$$

where t is an unknown parameter. Solving for x and y in Eq. (27) provides

$$x = \frac{a_t^2 u}{t + a_t^2} \quad \text{and} \quad y = \frac{b_t^2 v}{t + b_t^2} \tag{28}$$

For any (u, v), the closest point (x, y) will lie in the same quadrant since both points lie on the same line normal to the ellipse meaning u and x must have the same sign as well as v and y. Therefore, the constraints on t are $t > -a_t^2$ and $t > -b_t^2$. However, since $a_t > b_t$, the only constraint is $t > -b_t^2$. Substituting Eq. (28) into Eq. (26) yields to

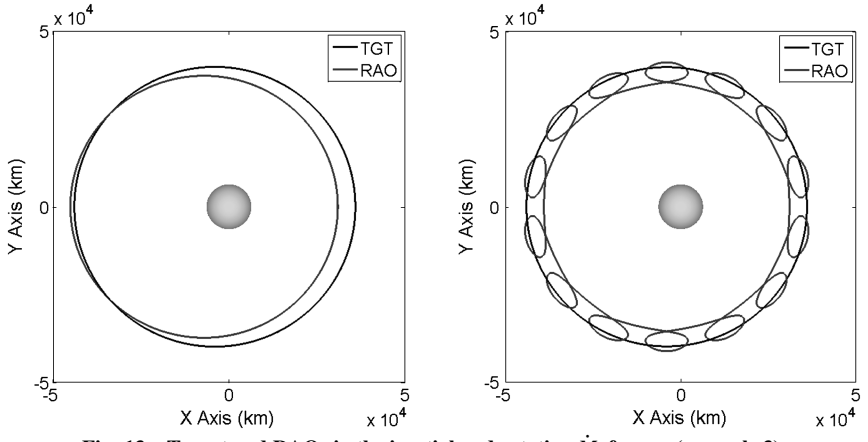

Fig. 13 Target and RAOs in the inertial and rotating $\dot{M}_t$ frames (example 3).

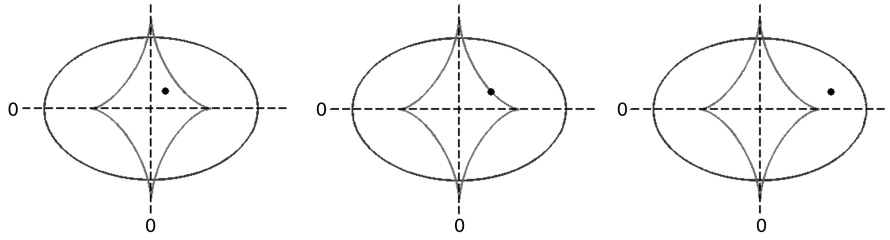

Fig. 14 Ellipse and evolute with (u, v) inside, on, and outside the evolute.

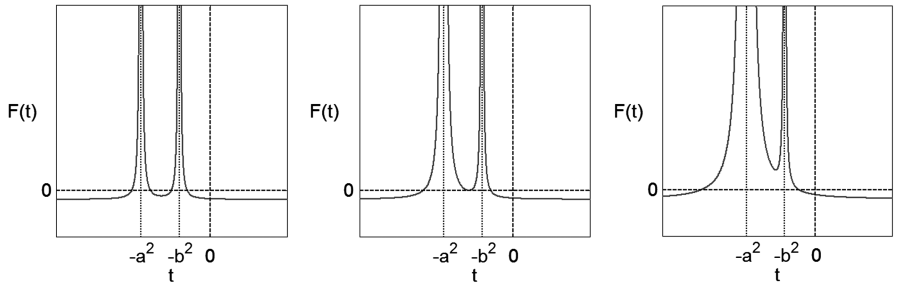

Fig. 15 $F(t)$ for (u, v) inside, on, and outside the evolute.

$$F(t) = \left(\frac{a_t u}{t + a_t^2}\right)^2 + \left(\frac{b_t v}{t + b_t^2}\right)^2 - 1 = 0 \tag{29}$$

$F(t)$ can be transformed into a quartic polynomial, therefore, $F(t)$ has four roots. The analysis of the three distinct graphs of $F(t)$ allows us to identify the correct root. In fact, as shown in Fig. 14, there are three distinct cases depending on where (u, v) is located with respect to the evolute of the ellipse (curve containing all the ellipse centers of curvature). The parametric equations of the evolute for an ellipse are

$$x = \frac{a_t^2 - b_t^2}{a_t}\cos^3 t \quad \text{and} \quad y = \frac{b_t^2 - a_t^2}{b_t}\sin^3 t$$

The three possibilities are shown in Fig. 14 and their corresponding graphs of $F(t)$ in Fig. 15 where (u, v) lies inside, on, and outside the evolute, respectively.

Of the four roots, the largest real root is always the only one greater than $-b^2$ as can be seen in Fig. 15. Substituting $t = -b^2$ into Eq. (28), the closest point on the ellipse, (x, y), to (u, v) is found. Using this solution the minimum distance, $d_{\min}$, is obtained by Pythagorean theorem $d_{\min} = \sqrt{(u-x)^2 + (v-y)^2 + z_r^{(t)^2}}$, where t is the largest real root of Eq. (29).

Figure 16 provides the minimum distance between the target orbits in one RAO period using the data provided in Sec. III.D. As it can be seen, the distance between the two orbits reaches but never exceeds $d_{\max}$ even with the maximum eccentricity and an inclination.

IV. Linear J_2 Perturbation

The theory so far presented is based on Keplerian two-body problem. Unfortunately, perturbations do exist and can destroy the RAO relative trajectory if the effects of the perturbations are different on the RAO than on the target orbit. As a first simplified model (linear J_2), let us consider two distinct effects: the nodal precession rate ($\dot{\Omega}$) and the argument of perigee rate ($\dot{\omega}$) differences. When these variations cannot be set to zero, control is needed to compensate them. The linear effects of the J_2 perturbations are ruled by the following equations:

$$\frac{\mathrm{d}\Omega}{\mathrm{d}t} = -\frac{3}{2}J_2\left(\frac{R_e}{p}\right)^2 n\cos i \tag{30}$$

$$\frac{\mathrm{d}\omega}{\mathrm{d}t} = \frac{3}{4}J_2\left(\frac{R_e}{p}\right)^2 n(5\cos^2 i - 1) \tag{31}$$

where $n = \sqrt{\frac{\mu}{a^3}}[1 + \frac{3}{4}J_2(\frac{R_e}{p})^2(2 - 3\sin^2 i)\sqrt{1-e^2}]$ is the perturbed mean motion, R_e the Earth's radius, and $p = a(1-e^2)$ the semilatus rectum. Using these equations, we can find the semimajor axis, eccentricity, and inclination combination allowing $\dot{\Omega}_r = \dot{\Omega}_t$ and $\dot{\omega}_r = \dot{\omega}_t$ or be near to these equalities to minimize station-keeping fuel requirements. The following two subsections summarize the Ω and ω maintenance, respectively.

A. Right Ascension of Ascending Node Maintenance

Consider the rate difference between the two precession rates, $\dot{\Omega}_d = \dot{\Omega}_t - \dot{\Omega}_r$, and its variation, $\Delta\Omega_d = \dot{\Omega}_d \Delta t$, in the time interval Δt. Depending on the sign of $\Delta\Omega_d$, two different cases where to apply the two-impulse maneuvers to keep $\Delta\Omega_d = 0$ are obtained. The first impulsive maneuver

$$\Delta v_1 = 2v_{\text{anti}}\sin\left(\frac{\Delta\vartheta}{2}\right) \quad \text{where } \Delta\vartheta = \tan^{-1}(\sin i \tan\Delta\Omega) \tag{32}$$

is performed at the antinode, where v_{anti} is the modulus of the velocity (at the antinode) while the second impulse is inclination correction to perform at one of the two nodal crossings. Figure 17 shows the spherical triangles for the two different cases. Using known spherical

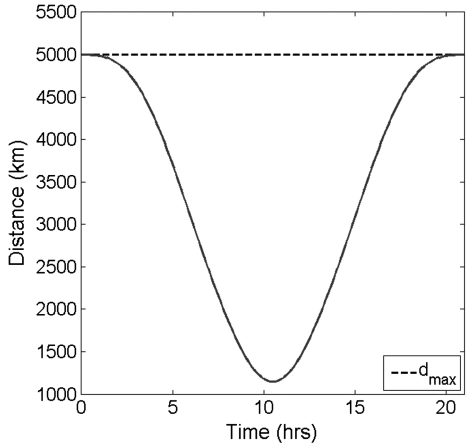

Fig. 16 Minimum distance to the target orbits for one RAO period (example 3).

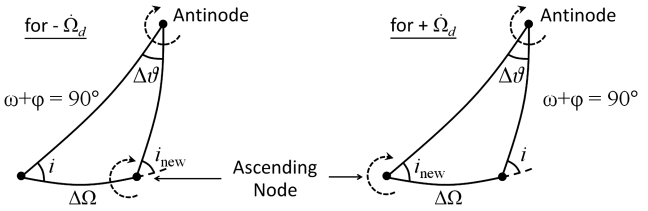

Fig. 17 Spherical geometry triangles associated to the two-impulse correction maneuver to compensate negative (left) or positive (right) $\Delta\Omega_d$.

Table 2 Angular rate differences and Δv (example 3)

Parameter, units	T_r, 20.54 h	T_{rep}, 11.98 days
$\dot{\Omega}_d$, deg /day	0.00403	0.00403
$\Delta\Omega_d$, deg	0.00345	0.0483
Δv_Ω, m/s	0.0176	0.246
$\dot{\omega}_d$, deg /day	−0.00783	−0.00783
$\Delta\omega_d$, deg	−0.00670	−0.0983
Δv_ω, m/s	0.0715	1.00
Δv_{tot}, m/s	0.0891	1.25

triangle law we can compute the orbital plane correction, $\Delta\vartheta$, compensating for the $\Delta\Omega_d$.

The first impulse compensates for the $\Delta\Omega_d$ variation but slightly changes also the orbit inclination (from i to i_{new}). For this reason the second impulsive correction is needed. The second impulsive correction is performed at whichever node (ascending or descending) has the smaller velocity, v_{node}. Therefore, the second impulse is $\Delta v_2 = 2v_{\text{node}} \sin(\frac{|i - i_{\text{new}}|}{2})$. Finally, the total cost to compensate $\Delta\Omega_d$ is $\Delta v_\Omega = \Delta v_1 + \Delta v_2$.

B. Argument of Perigee Maintenance

Just like for the $\Delta\Omega_d$ correction, the difference between the rate of perigee precession, $\dot{\omega}_d = \dot{\omega}_t - \dot{\omega}_r$, implies the need of the $\Delta\omega_d = \dot{\omega}_d \Delta t$ correction. The argument of perigee can be corrected by either applying a tangential thrust at true anomaly $\varphi = 90$ or 270° or by radial thrust applied at perigee ($\varphi = 0°$) or apogee ($\varphi = 180°$). The tangential thrust uses half as much fuel as the radial method but also changes the orbit semimajor axis and eccentricity, which must be then corrected. Therefore, the Δv_ω cost for perigee maintenance is

$$\text{tangential: } \Delta v_\omega = \left(\frac{e}{2}\sqrt{\frac{\mu}{p}}\right)\Delta\omega_d \quad \text{and}$$

$$\text{radial: } \Delta v_\omega = \left(e\sqrt{\frac{\mu}{p}}\right)\Delta\omega_d \tag{33}$$

C. Maintenance-Free RAOs

For an assigned target orbit it may be possible to create a RAO simultaneously satisfying $\dot{\Omega}_r = \dot{\Omega}_t$ and $\dot{\omega}_r = \dot{\omega}_t$. Using Eqs. (30) and (31), these two conditions become

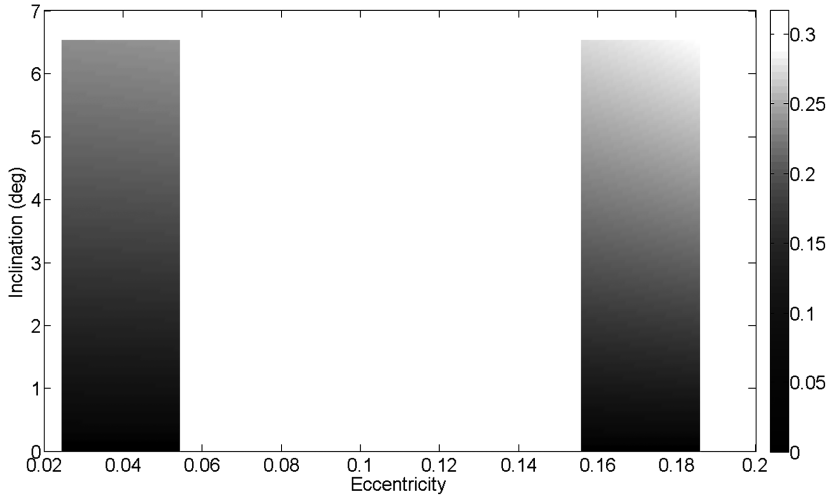

Fig. 18 Δv_Ω (m/s) for $T_{\text{rep}} = 11.98$ days.

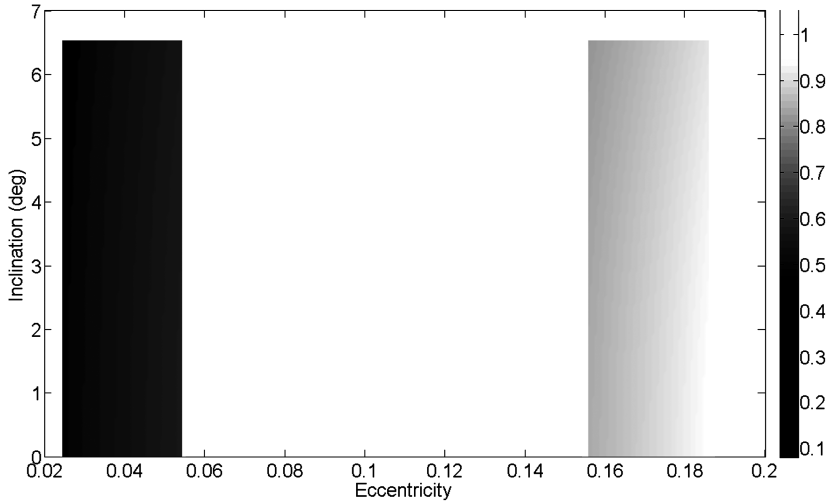

Fig. 19 Δv_ω (m/s) for $T_{\text{rep}} = 11.98$ days.

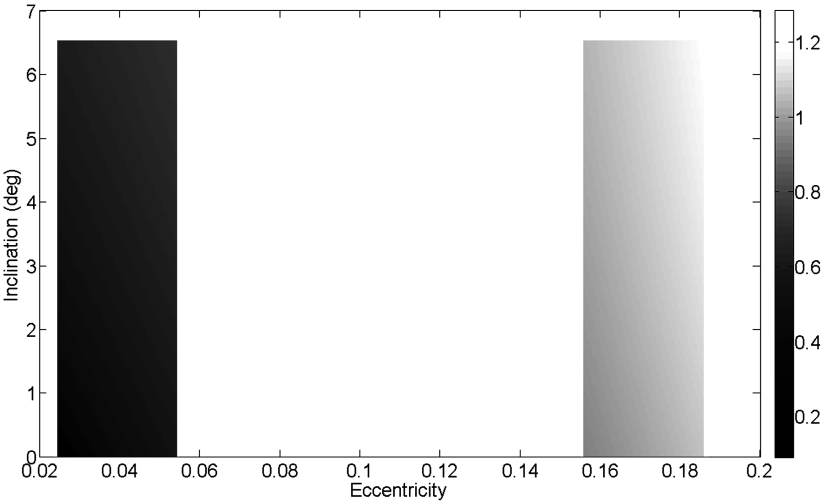

Fig. 20 Δv_{tot} (m/s) for $T_{\text{rep}} = 11.98$ days.

$$\dot{\Omega}_t = -\frac{3}{2}J_2\left(\frac{R_e}{p_r}\right)^2 n_r \cos i_r \quad \text{and}$$
$$\dot{\omega}_t = \frac{3}{4}J_2\left(\frac{R_e}{p_r}\right)^2 n_r(5\cos^2 i_r - 1) \tag{34}$$

For any compatible semimajor axis (a_r) obtained using Eq. (7), the system in Eq. (34) is a two equations in two unknown (e_r and i_r) system. Mathematically the solution exists. However, depending on the specific case under analysis, for any compatible semimajor axis the solution may not be feasible or be out of bounds. But even when the solution exists, the solution could be not optimal. In general, a tradeoff between the station-keeping costs and the efficiency of the observation system drives the solution selection process.

D. Example

Using the values provided in Sec. III.D, the angular rate differences of the RAO and the Δv costs needed to maintain them for two different time periods are provided in Table 2. Figures 18–20 show the different Δv_Ω, Δv_ω, and Δv_{tot} values, respectively, as a function of the eccentricity and inclination values.

V. Conclusions

This study introduces the theory of RAOs as a tool to design orbits to explore and observe the region around a given assigned target orbit. Motivations come from both civilian (mapping and monitoring systems) and military (surveillance systems) applications.

The theory is presented for circular and elliptical target orbit cases, respectively. The orbits proposed are compatible (resonant) with respect to the assigned target orbit in order to observe more some specific regions than others. When this is not needed, the compatibility condition can be taken out from the proposed theory.

Constraints on eccentricity and relative inclination are found for both circular and elliptical cases to satisfy distance constraints while the minimum distance to the target orbit is evaluated to provide a tool to quantify the optimality of different solutions. Some numerical examples are given to show, in the target orbit rotating frame, the spiraling behavior of the RAO relative trajectories around the target orbit. To compensate the effects of the perturbations, the nodal and argument of perigee orbit maintenance is briefly discussed and one example is given to estimate the orbital maintenance costs.

References

[1] Mill, J., O'Neill, R., Price, S., Romick, G., Uy, O., Gaposchkin, E., Light, G., Moore, W., Murdock, T., and Stair, A., Jr., "Midcourse Space Experiment: Introduction to the Spacecraft, Instruments, and Scientific Objectives," *Journal of Spacecraft and Rockets*, Vol. 31, No. 5, 1994, pp. 900–907. doi:10.2514/3.55673

[2] Stokes, G., von Braun, C., Sridharan, R., Harrison, D., and Sharma, J., "The Space-Based Visible Program," *Lincoln Laboratory Journal*, Vol. 11, No. 2, 1999, pp. 205–238.

[3] Gaposchkin, E., von Braun, C., and Sharma, J., "Space-Based Space Surveillance with the Space-Based Visible," *Journal of Guidance, Control, and Dynamics*, Vol. 23, No. 1, 2000, pp. 148–152. doi:10.2514/2.4502

[4] Sharma, J., "Space-Based Visible Space Surveillance Performance," *Journal of Guidance, Control, and Dynamics*, Vol. 23, No. 1, 2000, pp. 153–158. doi:10.2514/2.4503

[5] Capelle, K., and Sharma, J., "Geosynchronous Satellite Orbit Pattern: Improvements to SBV Geosynchronous Belt Search," Lincoln Lab. Rept. STK-255, April 2000.

[6] Mortari, D., Wilkins, M. P., and Bruccoleri, C., "The Flower Constellations," *Journal of the Astronautical Sciences*, Vol. 52, Jan.–June 2004, pp. 107–127.

[7] Mortari, D., and Wilkins, M. P., "The Flower Constellation Set Theory Part 1: Compatibility and Phasing," *IEEE Transactions on Aerospace and Electronic Systems*, Vol. 44, July 2008, pp. 953–963. doi:10.1109/TAES.2008.4655355

[8] Wilkins, M. P., and Mortari, D., "The Flower Constellation Set Theory Part 2: Secondary Paths and Equivalency," *IEEE Transactions on Aerospace and Electronic Systems*, Vol. 44, July 2008, pp. 964–976. doi:10.1109/TAES.2008.4655356

[9] Mortari, D., "Flower Constellations as Rigid Objects in Space," *ACTA Futura*, Vol. 2, 2006, pp. 7–22; also ESA Paper SP-633, First Innovative System Concepts Workshop, Noordwijk, The Netherlands, 2006, pp. 7–22.

[10] Abdelkhalik, O. O., and Mortari, D., "Two-Way Orbits," *Celestial Mechanics and Dynamical Astronomy*, Vol. 94, April 2006, pp. 399–410. doi:10.1007/s10569-006-9001-5

[11] Mortari, D., and Wilkins, M. P., "Dual-Compatible Flower Constellations," AAS/AIAA Space Flight Mechanics Meeting, Tampa, FL, American Astronomical Society Paper 06-202, 22–26 Jan. 2006.

[12] Bourgeois, S., and Mortari, D., "Rock-Around Orbits," AAS/AIAA Astrodynamics Specialist Conference, Pittsburgh, PA, American Astronomical Society Paper 09-343, 9–13 Aug. 2009.

[13] Bourgeois, S., "Rock-Around Orbits," M.S. Thesis, Texas A&M Univ., June 2009.